# Surface complexation of Pb(II) on amorphous iron oxide and manganese oxide: Spectroscopic and time studies

Ying Xu [a], Thipnakarin Boonfueng [a], Lisa Axe [a,*], Sungmin Maeng [a], Trevor Tyson [b]

[a] *Department of Civil and Environmental Engineering, New Jersey Institute of Technology, Newark, NJ 07102, USA*
[b] *Department of Physics, New Jersey Institute of Technology, Newark, NJ 07102, USA*

## Abstract

Hydrous Fe and Mn oxides (HFO and HMO) are important sinks for heavy metals and Pb(II) is one of the more prevalent metal contaminants in the environment. In this work, Pb(II) sorption to HFO ($Fe_2O_3 \cdot nH_2O$, $n = 1$–3) and HMO ($MnO_2$) surfaces has been studied with EXAFS: mononuclear bidentate surface complexes were observed on $FeO_6$ ($MnO_6$) octahedra with Pb–O distance of 2.25–2.35 Å and Pb–Fe(Mn) distances of 3.29–3.36 (3.65–3.76) Å. These surface complexes were invariant of pH 5 and 6, ionic strength $2.8 \times 10^{-3}$ to $1.5 \times 10^{-2}$, loading $2.03 \times 10^{-4}$ to $9.1 \times 10^{-3}$ mol Pb/g, and reaction time up to 21 months. EXAFS data at the Fe K-edge revealed that freshly precipitated HFO exhibits short-range order; the sorbed Pb(II) ions do not substitute for Fe but may inhibit crystallization of HFO. Pb(II) sorbed to HFO through a rapid initial uptake ($\sim$77%) followed by a slow intraparticle diffusion step ($\sim$23%) resulting in a surface diffusivity of $2.5 \times 10^{-15}$ cm²/s. Results from this study suggest that mechanistic investigations provide a solid basis for successful adsorption modeling and that inclusion of intraparticle surface diffusion may lead to improved geochemical transport depiction.
© 2006 Elsevier Inc. All rights reserved.

*Keywords:* Lead; Adsorption; Hydrous ferric oxide; Hydrous manganese oxide; Amorphous oxide; EXAFS; XANES; Intraparticle diffusion modeling

## 1. Introduction

Soils and sediments act as major sinks for heavy metals released from anthropogenic sources. Adsorption is one of the important processes that affect the transfer of heavy metals from the aqueous to solid phase thus influencing distribution, mobility, and bioavailability. Among soil components, iron and manganese oxides exist widely and have a high affinity and large capacity for metal contaminants [1–5]. As a result, these oxides are important phases in controlling heavy metal behavior in the environment. Studies [6–13] have shown that X-ray absorption spectroscopy (XAS) techniques can address speciation through depiction of the local coordination environment, which allows one to distinguish between adsorption and co-precipitation; corresponding surface complexation or precipitation reactions can be proposed accordingly for further modeling studies. There-fore XAS is an important tool in understanding and predicting the fate of heavy metals in the environment.

Pb(II) contamination is ubiquitous and has received much attention because of its toxicity. Many studies have been conducted on Pb(II) adsorption mechanisms on crystalline iron and aluminum oxides [14–21]. To construct an accurate description of the Pb(II)-oxide surface, Bargar et al. [12] studied Pb(II) sorption products and surface functional groups on iron oxides. They found that Pb(II) ions sorbed as mononuclear bidentate complexes to edges of $FeO_6$ octahedra on both goethite and hematite. Combined with bond-valence determination, the authors proposed that Pb(II) adsorption occurred primarily at $[Fe_{Fe}^{Fe} \rightarrow O^{-1/2}]$ and $[Fe–OH_2^{+1/2}]$ sites. Similar surface complexes have been observed for Al oxides [11,17]. However, Pb binding has been found to change with increasing sorption density: surface complexes on goethite shifted from bidentate corner-sharing to bidentate edge-sharing as the loading increased from 0.83 to 4.9 μmol Pb/m² [21]. On the other hand, Pb(II) polynuclear complexes were observed on $\gamma$-$Al_2O_3$ [15] and goethite [11,16]. Interestingly, Trivedi et al. [22] found

a mixture of bidentate edge- and monodentate corner-sharing Pb(II) complexes on 2-line ferrihydrite at pH 4.5 above which only the former was observed despite the extent of surface coverage.

Pb(II) uptake by goethite in the presence of various anions has also been investigated. Bargar et al. [13] proposed that the presence of $Cl^-$ has little effect on the Pb(II)/goethite and Pb(II)/$\gamma$-alumina surface complexes at pH 7, while Pb(II)–$Cl^-$-goethite ternary complexes were formed at pH $\leqslant$ 6. Recent studies indicated that first and second-shell distances for Pb sorption to goethite are essentially unchanged ($\Delta R < 0.03$ Å) by the presence of carbonate or sulfate [8,9,20]. While much work has been conducted with crystalline oxide surfaces, limited extended X-ray absorption fine structure (EXAFS) studies have been reported on amorphous iron oxides. Manceau et al. [23] observed that Pb(II) was adsorbed on HFO as mononuclear bidentate complexes on edges of $FeO_6$ octahedra based on a short-term contact time of three hours. Scheinost et al. [24] found that Cu and Pb formed similar edge-sharing inner-sphere sorption complexes when sorbed to 2-line ferrihydrite, this structure did not change as a function of time (up to 2 months), ferrihydrite morphology (with and without freeze-drying), and competing ions ($Cu^{2+}$). While Trivedi et al. [22] observed inner-sphere bidentate edge- and monodentate corner-sharing Pb(II) complexes, at constant pH, the configuration of the sorption complex was observed to be independent of the adsorbate concentration thus suggesting one average type of mechanism.

Furthermore, much fewer studies have been conducted on Pb adsorption to Mn oxides. Manceau et al. [23] proposed multinuclear surface complexes with a Pb oxy/hydroxy-like structure coordinating specifically with birnessite edges at 10.4% surface coverage. Recently, Manceau et al. [25] concluded that Pb sorption is independent of the surface loading (Pb/Mn atomic ratios range from 0.1 to 5.8%) on birnessite; similar to Zn, Pb predominantly sorbed to vacancy sites forming tridentate corner-sharing complexes. Matocha et al. [26] suggested a mononuclear corner-sharing Pb complex coordinated above and below the vacancy sites on birnessite with a Pb–Mn distance of 3.74 Å, while two Pb–Mn distances (3.31 and 3.87 Å) indicate both edge and corner-sharing mononuclear complexes formed on the manganite surface. More recently, Villalobos et al. [27] resolved Pb–Mn distances of ~3.5, 3.7, and 5.5 Å for Pb sorbed to a layered biogenic manganese oxide and attributed the results to double-corner- and triple-corner-sharing complexes at the external particle edges and interlayer sites above and below the vacancies, respectively. Pb adsorption on amorphous Mn oxide, one exhibiting no long-range order, has not yet been reported in literature. Meanwhile, although intraparticle diffusion into inner surfaces of soil has been observed [17,24,28–38], few studies [17,24,39] have been conducted in identifying the nature of internal sites especially for Pb/HFO and HMO systems. Pb(II) sorption mechanisms were found to be invariant with time on $\gamma$-$Al_2O_3$ [17] and 2-line ferrihydrite [24]; in both studies, there was no evidence of Pb precipitation.

Applying EXAFS analysis on samples of Pb sorbed to HFO and HMO as a function of time can address surface complexes formed during the diffusion process. Distinguishing the effect of time is especially important for amorphous oxides where phase transformation may impact sorption complexes. Determining surface complexes is critically important to successfully predicting metal adsorption to mineral surfaces using surface-complexation models. Because Pb adsorption onto amorphous HFO and HMO has not been systematically studied as a function of time, this work focuses on the transient sorption process using spectroscopic analysis of Pb adsorption at the HFO- and HMO-aqueous interfaces. In the sorption studies, systems were open to the atmosphere to simulate the natural environment.

## 2. Materials and methods

### 2.1. Iron oxide and manganese oxide synthesis and characterization

HFO ($Fe_2O_3 \cdot n H_2O$, $n = 1$–3, [40]) used in this study was synthesized following the method described by Dzombak and Morel [40], where 1 g L$^{-1}$ batches were prepared using $Fe(NO_3)_3 \cdot 9H_2O$ (>99.99%, Aldrich) and deionized (DI) water. Synthesis was conducted under turbulent conditions maintained by a motorized stirrer with a polyethylene coated impeller and purged with $N_2$ gas. For turbulent conditions used here and in the following, the Reynolds number (>$10^4$) was calculated based on rotation rate of the stir bar, impeller, or shaker and the associated characteristic length or diameter of the stir bar, impeller, or bottles being shaken. Ferric nitrate solutions were adjusted to pH 7–7.5 by dropwise addition of 10 N NaOH solution and aged for 4 h before adsorption studies.

HMO ($MnO_2$) was synthesized based on the method of Gadde and Laitinen [41]. An alkaline sodium permanganate ($NaMnO_4$, $4.6 \times 10^{-3}$ M) solution was prepared with a molar ratio 2:1 of NaOH to $NaMnO_4$. 1 g L$^{-1}$ batches of HMO were precipitated by slowly adding manganese nitrate ($Mn(NO_3)_2$) to the alkaline $NaMnO_4$ with a final molar ratio of 3:2. The solution was mixed under turbulence by a magnetic stirrer for 3 h and was purged with $N_2$ to remove $CO_2$. The suspension was then centrifuged and rinsed with DI water, after which the oxide was redispersed in a $1.5 \times 10^{-2}$ M $NaNO_3$ solution prior to use.

Freshly prepared HFO and HMO have been characterized on aqueous and as well as freeze-dried samples in earlier studies [32,35]. The X-ray diffractograms of HFO and HMO are broad and flat indicative of amorphous structures. For HFO, the porosity was 0.5 and the pore size distribution from Hg porosimetry showed a mean pore radius less than 5 nm [32]. HMO had a porosity of 0.3 with two modes of pore radii at 2.1 and 6.1 nm (with $N_2$ desorption method) [35]. For both oxides, scanning electron micrographs suggested aggregated particles which were spherical with highly irregular topography [32,35]. The particle size distribution in the aqueous phase was in the range 0.5–350 μm with modes at approximately 6.5 and 90 μm for HFO and in the range 0.5–400 μm with a mode at approximately 15 μm for HMO [32,35]. Therefore, the freshly precipitated HFO and HMO samples, which were used in the following adsorption studies, aggregate into larger spherical particles in aqueous phase, where layers of water adsorb on the meso- and/or micropores pore walls.

Goethite used as a standard for Fe EXAFS was synthesized and characterized in earlier work [39]; hematite was purchased from Alfa Aesar (99.8% purity).

## 2.2. Sample preparation

In all adsorption studies, the bulk aqueous phase concentration of Pb was below the solubility limit for hydrocerussite, $Pb_3(OH)_2(CO_3)_2$, the thermodynamically stable mineral [42,43]. Ionic strength (IS), pH, and $Pb^{2+}$ concentration were adjusted with $NaNO_3$, $HNO_3$, and $NaOH$, and a stock solution of $Pb(NO_3)_2$. Turbulence was maintained to eliminate resistance due to external mass transfer. All solutions were prepared from Milli-Q Type I DI water. $Pb(NO_3)_2$ stock solutions were prepared using Aldrich high-purity (99.999%) reagent maintained at pH 2 and stored in Nalgene (r) high density polypropylene containers.

Pb(II) sorption was studied open to the atmosphere with experimental conditions listed in Table 1. The amount of metal adsorbed was calculated from a mass balance by subtracting the final aqueous concentration from the initial one. Because the BET surface area is measured on freeze-dried particle, it does not necessarily represent that of the hydrous one in the aqueous environment; metal loadings on the hydrated samples were not normalized to the surface area. Metal concentrations were analyzed with a Beckman Liquid Scintillation System (Model LS6500) using an isotope-tagged ($Pb^{210}$) metal-nitrate stock solution to adjust the concentration. Therefore, duplicate samples were prepared: one tagged with $Pb^{210}$ to measure the amount of Pb sorbed; and the other not tagged for XAS analyses. The effect of pH, ionic strength, and Pb loading were investigated using short-term samples, where a pseudo-equilibrium was observed after 4 h of contact time. These samples represent sorption to the external surface of the oxides. A series of long-term samples (from 1 to 21 months) were prepared from constant boundary condition (CBC) experiments to study the transient sorption process [32]. CBC studies are convenient to investigate diffusion in micropores where the aqueous metal concentration as well as pH are maintained constant. Compared to the decreasing metal concentration in typical adsorption studies, diffusion can be observed over a convenient time frame. CBC studies were conducted in 1 L Nalgene bottles, the bulk aqueous concentration of metal ions was maintained approximately constant by monitoring and adding adsorbate as necessary. All XAS samples were in the form of wet paste using centrifugation (12000 RPM for 20 min with the Sorvall RC-28S centrifuge) for solid/liquid separation and without any further treatment to maintain conditions studied.

Table 1
Sample preparation conditions

| Sample | pH | IS | Solid ($g\,L^{-1}$) | $[Pb]_0$ (M) | $[Pb]_{eq}$ (M) | $Pb_{ads}$ ($mol\,g^{-1}$) | Reaction time |
|---|---|---|---|---|---|---|---|
| Pb/HFO $10^{-3}$ mol/g, pH 6, IS $10^{-3}$ | 6 | $2.8 \times 10^{-3}$ | 0.1 | $4 \times 10^{-4}$ | $5.9 \times 10^{-5}$ | $3.41 \times 10^{-3}$ | 4 h |
| Pb/HFO $10^{-4}$ mol/g, pH 6, IS $10^{-3}$ | 6 | $5.6 \times 10^{-3}$ | 0.2 | $5 \times 10^{-5}$ | $9.0 \times 10^{-6}$ | $2.04 \times 10^{-4}$ | 4 h |
| Pb/HFO $10^{-4}$ mol/g, pH 5, IS $10^{-3}$ | 5 | $5.6 \times 10^{-3}$ | 0.2 | $5 \times 10^{-5}$ | $9.4 \times 10^{-6}$ | $2.03 \times 10^{-4}$ | 4 h |
| Pb/HFO $10^{-3}$ mol/g, pH 5, IS $10^{-3}$ | 5 | $5.6 \times 10^{-3}$ | 0.2 | $4 \times 10^{-4}$ | $1.6 \times 10^{-5}$ | $1.92 \times 10^{-3}$ | 4 h |
| Pb/HFO $10^{-3}$ mol/g, pH 5, IS $10^{-2}$ | 5 | $5.6 \times 10^{-2}$ | 0.2 | $4 \times 10^{-4}$ | $1.8 \times 10^{-5}$ | $1.91 \times 10^{-3}$ | 4 h |
| Pb/HFO, 1 month $10^{-3}$ mol/g, pH 5, IS $10^{-2}$ | 5 | $1.4 \times 10^{-2}$ | 0.3 | $5 \times 10^{-4}$ | $1.1 \times 10^{-4}$ | $1.75 \times 10^{-3}$ | 1 month |
| Pb/HFO, 4 months $10^{-3}$ mol/g, pH 5, IS $10^{-2}$ | 5 | $1.4 \times 10^{-2}$ | 0.3 | $5 \times 10^{-4}$ | $9.7 \times 10^{-5}$ | $1.80 \times 10^{-3}$ | 4 months |
| Pb/HFO, 9 months $10^{-3}$ mol/g, pH 5, IS $10^{-2}$ | 5 | $1.4 \times 10^{-2}$ | 0.3 | $5 \times 10^{-4}$ | $1.2 \times 10^{-4}$ | $1.72 \times 10^{-3}$ | 9 months |
| Pb/HFO, 14 months $10^{-3}$ mol/g, pH 5, IS $10^{-2}$ | 5 | $1.4 \times 10^{-2}$ | 0.3 | $5 \times 10^{-4}$ | $1.2 \times 10^{-4}$ | $1.73 \times 10^{-3}$[a] | 14 months |
| Pb/HFO, 21 months $10^{-3}$ mol/g, pH 5, IS $10^{-2}$ | 5 | $1.4 \times 10^{-2}$ | 0.3 | $5 \times 10^{-4}$ | $1.2 \times 10^{-4}$ | $1.73 \times 10^{-3}$[a] | 21 months |
| Pb/HMO $10^{-2}$ mol/g, pH 5, IS $10^{-2}$ | 5 | $1.5 \times 10^{-2}$ | 0.1 | $1 \times 10^{-3}$ | $9.0 \times 10^{-5}$ | $9.10 \times 10^{-3}$ | 4 h |
| Pb/HMO $10^{-3}$ mol/g, pH 6, IS $10^{-2}$ | 6 | $1.5 \times 10^{-2}$ | 0.2 | $3 \times 10^{-4}$ | $3.0 \times 10^{-5}$ | $1.35 \times 10^{-3}$ | 4 h |
| Pb/HMO, 1 month $5 \times 10^{-4}$ mol/g, pH 6, IS $10^{-2}$ | 6 | $1.5 \times 10^{-2}$ | 0.1 | $5 \times 10^{-5}$ | $6.0 \times 10^{-7}$ | $5.40 \times 10^{-4}$ | 1 month |
| Pb/HMO, 4 months $6 \times 10^{-4}$ mol/g, pH 6, IS $10^{-2}$ | 6 | $1.5 \times 10^{-2}$ | 0.1 | $5 \times 10^{-5}$ | $6.0 \times 10^{-7}$ | $6.00 \times 10^{-4}$ | 4 months |

[a] Data measured on the 392nd day. System was kept in turbulence and XAS samples were taken in the 14th and 21st months.

## 2.3. XAS data collection and analysis

The XAS data were collected at beamline X-11A for Pb and X-11B for Fe at the National Synchrotron Light Source (NSLS), Brookhaven National Laboratory. The storage ring was operated at 2.81 GeV beam energy with a beam current in the range 100–300 mA. Silicon(111) double-crystal monochromators were used for both beamlines. The incident beam ($I_0$) was detuned by 30% to reject high-energy harmonics. Data were collected in both transmission and fluorescence modes. The $I_0$ ion chamber was filled with $N_2(g)$ and the fluorescence signal ($I_f$) was collected using a Lytle detector filled with Ar gas. The transmission signal ($I_t$) was measured with an ion chamber containing a $N_2(g)$ and $Ar(g)$ gas mixture adjusted to absorb approximately 60% of the incoming X-rays. Pb and Fe foils were used as references for energy calibration. EXAFS spectra were collected from 12,855 to 13,602 eV over the Pb $L_{III}$-edge and from 6912 to 7857 eV over the Fe K-edge. At least five scans for Fe and typically 10–20 scans for Pb were collected. The analysis was carried out on the averaged fluorescence data for Pb at the $L_{III}$-edge and transmission data for Fe at the K-edge. All EXAFS data were collected at room temperature.

The XAS data were analyzed with WinXAS 2.3 following standard procedures [44]. For each scan, the background was fitted with a linear polynomial through the pre-edge region and subtracted. The edge jump of the background-corrected XAS spectra was then normalized to one by refining 100–200 eV above the edge with a zero order polynomial and normalizing the spectra to the ordinate value of this polynomial. The energy threshold ($E_0$) of the absorption spectrum was determined from the first inflection point of the edge region and was used to convert the absorption spectrum from energy to $k$-space. A cubic spline function with three knots was applied to account for the isolated atomic absorption $\mu_0(E)$. The EXAFS function ($\chi(k)$) was obtained after subtracting $\mu_0(E)$ from the absorption of the atom in condensed matter. The $\chi(k)$ spectra were weighted by $k^3$ to enhance the higher $k$-space data and then Fourier transformed using the Bessel window function to produce the radial structural function (RSF). The RSF was not corrected for phase shift. EXAFS fitting of the RSF was conducted using theoretical phase shift and amplitude functions calculated by the FEFF 7 code [45]. Parameters were all floated (except for amplitude reduction factor, $S_0^2$, and for Fe K-edge, the coordination number was fixed based on XRD data); therefore, the resulting coordination numbers (not fixed ones), distances, $E_0$ shifts, and Debye–Waller factors ($\sigma^2$) reflect the best fits. Errors were assessed by fitting the spectra averaged over subgroups of scans.

## 2.4. XRD analysis

Mineralogy was determined by powder X-ray diffraction (XRD) using a Rigaku MiniFlex diffractometer. XRD data were collected using $FeK\alpha$ radiation via continuous scan in 0.02° $2\theta$ steps with a count time of 12 s step$^{-1}$. Samples were prepared as smear mounts with methanol on zero background quartz slides (typically 10–15 mg of sample). Mounted samples were allowed to air dry prior to data collection. The NIST SRM 640b (silicon) was used for external calibration of goniometer angular position. Peak identification for crystalline phases was achieved by reference to the International Centre for Diffraction Data (ICDD) Powder Diffraction File database [46]. Identification of 2-line ferrihydrite was carried out based on the work of Stanjek and Weidler [47]. Semi-quantitative estimates of phase percentages were determined by whole-pattern fitting using synthetic goethite and hematite.

## 3. Results and discussion

### 3.1. Pb EXAFS of Pb/HFO samples

Pb adsorption mechanisms on freshly precipitated HFO samples as a function of pH, ionic strength, Pb loading, and time have been studied. The EXAFS spectra collected for Pb standards (PbO, $PbCO_3$, and aqueous $Pb(NO_3)_2$) are compared to Pb/HFO adsorption samples (Fig. 1). The $\chi(k)k^3$ spectra of PbO and $PbCO_3$ are similar to that observed by others [7,11,19] and the fitting results (Table 2) are consistent with XRD. The $\chi(k)k^3$ spectra of aqueous $Pb(NO_3)_2$ solution is characterized by an oscillation dominated by backscattering from first-shell oxygen atoms around the central Pb atom (Fig. 1). The RSF (Fig. 1) clearly demonstrates this Pb–O contribution fitted with $7.0 \pm 1.4$ O atoms at $2.50 \pm 0.08$ Å. This octahedral structure represents that of fully hydrated Pb(II), as greater than 99% of the total Pb exists as $Pb^{2+}$ in this aqueous sample [43]. This result is consistent with other studies [11,48].

All spectra of Pb/HFO sorption samples are different from those of $Pb_3(OH)_2(CO_3)_2$ [8,11], PbO, $PbCO_3$, and aqueous $Pb(NO_3)_2$ (Figs. 1 and 2), suggesting unique structures as compared to these standards. Overall, the spectra are dominated by the backscattering from a first shell of O atoms and beat features at 4.5–5.0 and 6.5–8.5 Å$^{-1}$ indicative of a heavier backscatter from second shell contributions. The $\chi(k)k^3$ spectra were Fourier transformed over the range 2.8–9.5 Å$^{-1}$ and fitted over the range 0.45–3.58 Å with a Fe-substituted PbO model generated theoretically using FEFF7 [45]. The RSFs show two peaks at ∼1.9 and ∼2.9 Å (Fig. 1), and fitting (Table 3) reveals 1.3–2.9 O atoms at 2.25–2.30 Å for the first shell. The second shell could only be fit with Fe atoms and resulted in 0.9–2.2 Fe atoms at 3.29–3.34 Å. The experimental magnitude and phase were reproduced by the fitting (Figs. 1 and 2). However, the larger Debye–Waller factor for the second shell (Table 3) suggests greater variation in the Pb–Fe distances than those for Pb–O.

The absence of Pb backscatters around the central atom suggests that the adsorbed Pb(II) ions on HFO are isolated mononuclear sorption complexes. The fitted Pb–O coordination numbers and distances in the sorption samples are consistent with that of Bargar et al. [12] suggesting Pb(II) ions may exist in a distorted trigonal pyramidal structure [12]. The relatively small coordination number for O atoms in the fit may be explained with the positional disorder of the first shell O atoms, backscattering from which may interfere destructively [11]. Water molecules present at the solid/liquid interface may act as ligands of the adsorbed Pb(II) ions, but the corresponding Pb–O
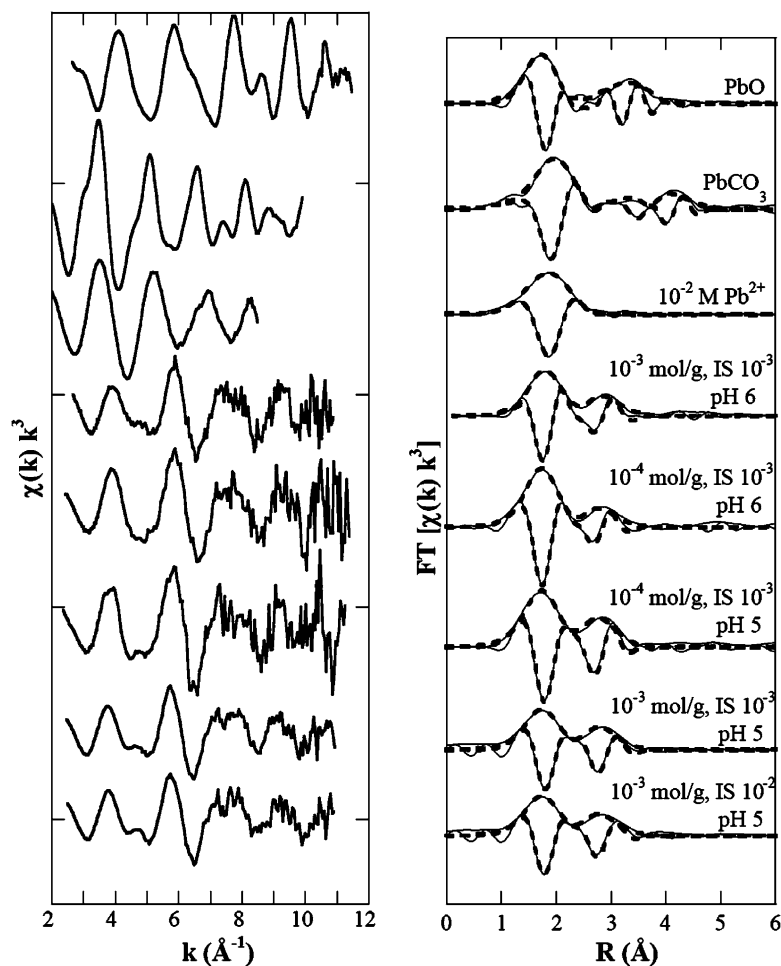
Fig. 1. EXAFS spectra and Fourier transform (magnitude and imaginary part) of Pb standards and 4-h Pb/HFO sample at Pb $L_{III}$-edge. FT was performed over range: PbO 3.0–10.8 $Å^{-1}$, $PbCO_3$ 2.08–9.79 $Å^{-1}$, $Pb^{2+}$ 2.26–8.48 $Å^{-1}$, Pb/HFO 2.8–9.5 $Å^{-1}$; PbO was fitted over 0.74–3.95 Å, $PbCO_3$ 0.46–4.69 Å, $Pb^{2+}$ 0.42–3.0 Å, and Pb/HFO 0.45–3.58 Å. Dashed lines represent fits.

Table 2
EXAFS results of Pb standards at Pb $L_{III}$-edge: FT was performed over range: PbO 3.0–10.8 $Å^{-1}$, $PbCO_3$ 2.08–9.79 $Å^{-1}$, $Pb^{2+}$ 2.26–8.48 $Å^{-1}$; PbO was fitted over range 0.74–3.95 Å, $PbCO_3$ 0.46–4.69 Å, and $Pb^{2+}$ 0.42–3.0 Å

| Sample | Atom | $N$ | $R$ (Å) | $\sigma^2$ ($Å^2$) | $\Delta E_0$ (eV) | Residual |
|---|---|---|---|---|---|---|
| $\beta$-PbO (XRD) [65] | O | 2 | 2.24 | | | |
| | O | 2 | 2.48 | | | |
| | Pb | 4 | 3.54 | | | |
| $PbCO_3$ (XRD) [66] | O | 1 | 2.62 | | | |
| | O | 2 | 2.66 | | | |
| | O | 2 | 2.68 | | | |
| | O | 2 | 2.71 | | | |
| | O | 2 | 2.77 | | | |
| | Pb | 6 | 4.13 | | | |
| | Pb | 6 | 4.18 | | | |
| PbO | O | $1.9 \pm 0.4$ | $2.23 \pm 0.02$ | $0.006 \pm 0.001$ | $-11.68 \pm 1.09$ | 11.78 |
| | Pb | $1.4 \pm 0.3$ | $3.53 \pm 0.02$ | $0.005 \pm 0.001$ | | |
| $PbCO_3$ | O | $11.2 \pm 2.6$ | $2.60 \pm 0.02$ | $0.025 \pm 0.003$ | $-1.09 \pm 2.27$ | 15.54 |
| | Pb | $9.6 \pm 1.9$ | $4.15 \pm 0.02$ | $0.018 \pm 0.001$ | | |
| $Pb(NO_3)_2$ | O | $7.0 \pm 1.4$ | $2.50 \pm 0.08$ | $0.023 \pm 0.001$ | $-7.48 \pm 0.44$ | 6.64 |

*Note.* $N$, coordination number; $R$, interatomic distance; $\sigma^2$, Debye–Waller factor; $\Delta E_0$, edge shift.

distances should be greater than 2.75 Å [11]. Other EXAFS investigations [22–24] reported that the adsorbed Pb(II) on ferrihydrite results in two O atoms at 2.3 Å and less than one to two Fe atoms at around 3.3 Å. The fitting results of this study are similar with those previous studies. Bargar et al. [12] proposed that Pb–Fe distances of 2.91–3.49 Å reflect bidentate
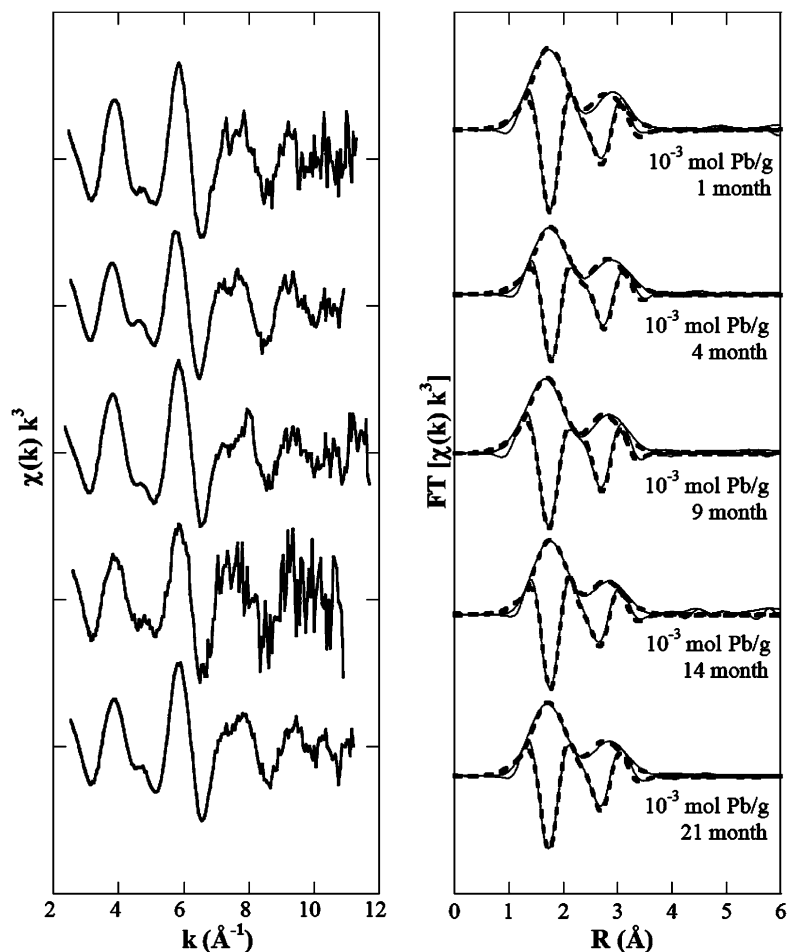
Fig. 2. EXAFS spectra and Fourier transform (magnitude and imaginary part) of Pb/HFO samples at pH 5 and IS $10^{-2}$ as a function of time at Pb $L_{III}$-edge. FT was performed over range 2.8–9.5 Å$^{-1}$, fitted over 0.45–3.58 Å. Dashed lines represent fits.

adsorption to edges of FeO$_6$ octahedra. EXAFS analysis of our Pb/HFO samples suggests that upon adsorption, Pb ions lose at least part of their waters of hydration and form mononuclear bidentate complexes at the edges of FeO$_6$ octahedra.

Pb/HFO sorption samples were prepared at pH 5 and 6, ionic strength from $10^{-3}$ to $10^{-2}$, loading from $2.04 \times 10^{-4}$ to $3.41 \times 10^{-3}$ mol Pb/g HFO, and reaction time of 4 h to 21 months; the similarity in $\chi(k)k^3$ spectra and the fitting results of all these samples indicate similar local structures. Therefore Pb adsorption to HFO may be described with one average type of mechanism under the experimental conditions tested. Time studies resulted in a 23% increase in adsorption which is attributed to intraparticle diffusion; a unique coordination environment for internal sites would potentially impact the signal. On the other hand, aging could result in solid solution formation, precipitation, and crystallization of the oxide also affecting the Pb(II) local structure. Spectra (Fig. 2) suggest however that the sorption complex remained unchanged with time and therefore the internal and external adsorption sites are approximately equivalent. One assumption in earlier modeling efforts [32,33, 36,38] was that the adsorption sites located along the micropore walls are no different from ones on the external surface; this assumption is verified in this current Pb/amorphous HFO EXAFS study.

The conversion of HFO to goethite and hematite has been reported to be slow at temperatures below 20 °C, and is further retarded by adsorbed species [49–51]. The effect of Pb(II) on the transformation of HFO to goethite or hematite during the long-term CBC studies is addressed in Section 3.2.

### 3.2. Fe XAS of iron oxides and Pb/HFO samples

Three iron oxides, freshly prepared HFO, goethite ($\alpha$-FeOOH), and hematite ($\alpha$-Fe$_2$O$_3$), and two Pb/HFO samples (reacted for 4 h and 21 months) were analyzed with XAS to study the crystallization of HFO. In the X-ray absorption near edge structure (XANES) analysis (Fig. 3), the spectra of HFO and goethite were adjusted to correct for energy calibration at the Fe K-edge. All samples (Fig. 3) have a similar pre-edge feature suggesting the presence of defects in FeO$_6$ octahedra [52]. The more pronounced pre-edge structure for HFO samples indicates a greater degree of defects. Tetrahedrally coordinated Fe atoms produce a well-resolved shoulder (at about three fifths of the edge height) before maximum edge peak [52]. The absence of such a feature in the spectra of HFO and its similarity to that of goethite, which exhibits octahedral (FeO$_6$) structure [53], suggest HFO and Pb/HFO samples too have octahedral structure. This result is consistent with other studies [23,52,54–58].

Table 3
EXAFS results of Pb/HFO samples at Pb $L_{III}$-edge: FT was performed over range 2.8–9.5 $Å^{-1}$, fitted over range 0.45–3.58 Å

| Sample | Atom | $N$ | $R$ (Å) | $\sigma^2$ ($Å^2$) | $\Delta E_0$ (eV) | Residual |
|---|---|---|---|---|---|---|
| Pb/HFO | O | $1.3 \pm 0.3$ | $2.30 \pm 0.02$ | $0.003 \pm 0.001$ | $-8.84 \pm 2.47$ | 7.40 |
| $10^{-3}$ mol/g, pH 6, IS $10^{-3}$ | Fe | $2.2 \pm 0.9$ | $3.34 \pm 0.02$ | $0.019 \pm 0.005$ | | |
| Pb/HFO | O | $2.3 \pm 0.8$ | $2.27 \pm 0.03$ | $0.007 \pm 0.002$ | $-13.86 \pm 2.93$ | 10.40 |
| $10^{-4}$ mol/g, pH 6, IS $10^{-3}$ | Fe | $0.9 \pm 1.2$ | $3.29 \pm 0.06$ | $0.010 \pm 0.008$ | | |
| Pb/HFO | O | $2.9 \pm 0.6$ | $2.29 \pm 0.02$ | $0.009 \pm 0.002$ | $-14.98 \pm 1.97$ | 9.76 |
| $10^{-4}$ mol/g, pH 5, IS $10^{-3}$ | Fe | $1.4 \pm 1.1$ | $3.29 \pm 0.02$ | $0.011 \pm 0.007$ | | |
| Pb/HFO | O | $1.9 \pm 0.4$ | $2.29 \pm 0.02$ | $0.007 \pm 0.025$ | $-15.43 \pm 1.31$ | 11.60 |
| $10^{-3}$ mol/g, pH 5, IS $10^{-3}$ | Fe | $1.6 \pm 0.5$ | $3.33 \pm 0.02$ | $0.013 \pm 0.003$ | | |
| Pb/HFO | O | $1.8 \pm 0.4$ | $2.29 \pm 0.02$ | $0.008 \pm 0.003$ | $-14.80 \pm 2.98$ | 12.23 |
| $10^{-3}$ mol/g, pH 5, IS $10^{-2}$ | Fe | $1.8 \pm 0.6$ | $3.34 \pm 0.02$ | $0.015 \pm 0.007$ | | |
| Pb/HFO, 1 month | O | $2.2 \pm 0.4$ | $2.28 \pm 0.02$ | $0.008 \pm 0.055$ | $-12.22 \pm 0.65$ | 10.95 |
| $10^{-3}$ mol/g, pH 5, IS $10^{-2}$ | Fe | $2.0 \pm 0.5$ | $3.32 \pm 0.02$ | $0.016 \pm 0.003$ | | |
| Pb/HFO, 4 months | O | $1.4 \pm 0.3$ | $2.30 \pm 0.02$ | $0.005 \pm 0.001$ | $-12.14 \pm 0.27$ | 9.21 |
| $10^{-3}$ mol/g, pH 5, IS $10^{-2}$ | Fe | $2.1 \pm 0.4$ | $3.36 \pm 0.02$ | $0.017 \pm 0.003$ | | |
| Pb/HFO, 9 months | O | $2.5 \pm 0.5$ | $2.25 \pm 0.02$ | $0.010 \pm 0.001$ | $-15.86 \pm 0.65$ | 11.60 |
| $10^{-3}$ mol/g, pH 5, IS $10^{-2}$ | Fe | $1.3 \pm 0.3$ | $3.30 \pm 0.02$ | $0.011 \pm 0.001$ | | |
| Pb/HFO, 14 months | O | $1.3 \pm 0.3$ | $2.29 \pm 0.04$ | $0.004 \pm 0.002$ | $-11.16 \pm 4.88$ | 7.64 |
| $10^{-3}$ mol/g, pH 5, IS $10^{-2}$ | Fe | $1.9 \pm 2.1$ | $3.31 \pm 0.05$ | $0.017 \pm 0.009$ | | |
| Pb/HFO, 21 months | O | $1.8 \pm 0.4$ | $2.27 \pm 0.03$ | $0.007 \pm 0.002$ | $-12.99 \pm 4.10$ | 9.46 |
| $10^{-3}$ mol/g, pH 5, IS $10^{-2}$ | Fe | $2.1 \pm 0.4$ | $3.32 \pm 0.04$ | $0.017 \pm 0.001$ | | |

*Note.* $N$, coordination number; $R$, interatomic distance; $\sigma^2$, Debye–Waller factor; $\Delta E_0$, edge shift. An $S_0^2$ of 0.91 was used to account for self-absorption based on the ratio of fluorescence to transmission data for aqueous $Pb^{2+}$.
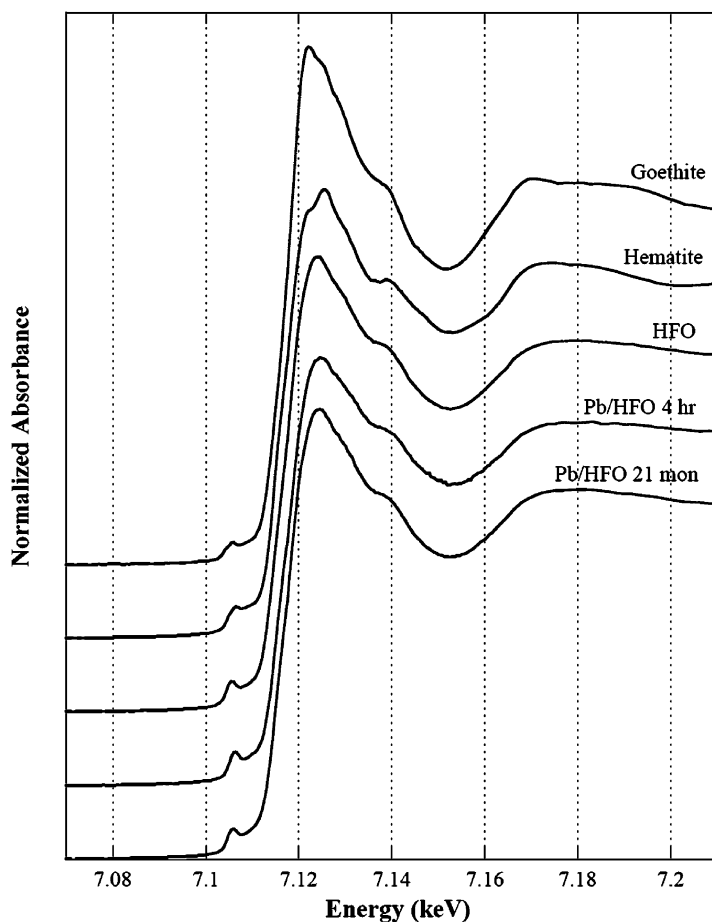


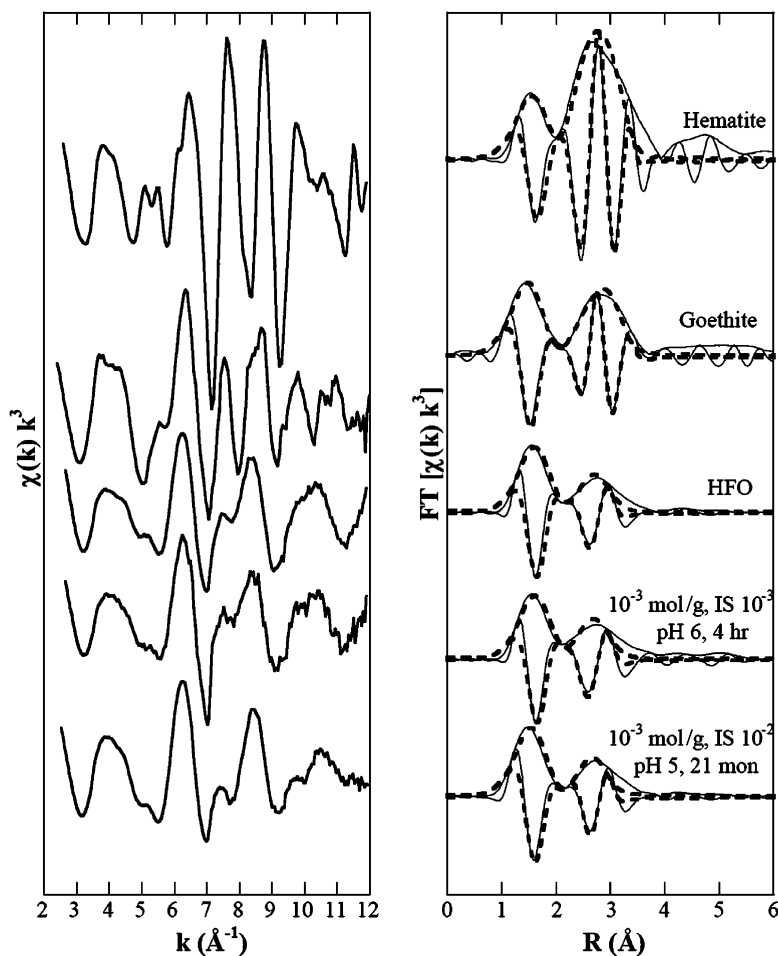Fig. 3. Fe K-edge XANES spectra of iron oxides.

Fig. 4. EXAFS spectra and Fourier transform (magnitude and imaginary part) of iron oxides and Pb/HFO samples at Fe K-edge. FT was performed over range: hematite 2.83–11.42 Å$^{-1}$, goethite 2.63–11.19 Å$^{-1}$, HFO and Pb/HFO sorption samples 2.86–11.77 Å$^{-1}$. Hematite was fitted over 0.53–3.95 Å, goethite 0.63–3.76 Å, HFO and Pb/HFO samples 0.52–3.91 Å. Dashed lines represent fits.

Compared to hematite, goethite and HFO appear to have less features in the XANES spectra. Although relatively low in intensity, the shape of the edge crest of HFO is closer to that of goethite. Also, similar edge crests were observed for HFO and Pb-sorbed HFO samples (aged for 4 h and 21 months) indicating a similar local structure even as a function of reaction time.

The EXAFS spectra (Fig. 4) of hematite and goethite show backscattering from multiple Fe atoms at different distances. The first two RSF peaks of each spectrum (Fig. 4) can be fitted with O and two subshells of Fe atoms, respectively, for which the coordination numbers were fixed based on XRD results [59,60]. Overall the fitting results are consistent with XRD data (Table 4). Although multiple Fe–Fe distances exist for hematite and goethite (Table 4), the fitting results represent an averaged local structure. For hematite and goethite, the edge-sharing of FeO$_6$ octahedra produces Fe–Fe distances of 2.97–3.28 Å and that for double corner-sharing is 3.37–3.70 Å [56]. Therefore, the Fe–Fe distance of 3.35–3.36 Å in the fitting results (Table 4) suggest the presence of double corner-sharing between FeO$_6$ octahedra, which is necessary for crystal growth.

The spectrum of HFO (Fig. 4) show beats at 4.5, 5.2, 7.5, and 9.2–9.9 Å$^{-1}$ indicative of Fe atoms around the central one. The RSF (Fig. 4) reveals two well-defined peaks that can be fitted

with O and Fe atoms, respectively. Many studies have reported an octahedral coordination environment [23,52,54–56,58] for Fe atoms in HFO; the number of O atoms was thus fixed during fitting. Considering error, the fitted Fe–O, Fe–Fe distances are similar to that of goethite (Table 4). The Fe–Fe distance of 3.08 ± 0.02 Å (Table 4) suggests the presence of edge-sharing polymers in HFO without corner-sharing.

The $\chi(k)k^3$ spectra (Fig. 4), RSF (Fig. 4), and the fitting results (Table 4) of 4-h and 21-month Pb/HFO samples are similar to those of HFO. Fits of the 4-h and 21-month samples were also checked in $k$-space after back Fourier transform; overall, the fits are consistent with the data. The amplitudes of the fits are greater in lower $k$-space than those of the data which may be due to fixing the first shell coordination number at 6. As shown in Fig. 4, the peak-to-valley amplitudes were noted to differ between the 4-h and 21-month samples within the $k$-range of 6–9 Å$^{-1}$. Because XRD analysis of a 29-month sample (Fig. 5) suggests dominance of ferrihydrite with trace hematite and goethite, linear combinations of the 4-h sample, hematite, and goethite spectra were evaluated to simulate the 21-month sample; however, based on a principle component analysis, the 4-h sample represents that of the 21-month sample over any other fractional combination.

Table 4
EXAFS results of iron oxides and Pb/HFO samples at Fe K-edge

| Sample | Atom | $N$ | $R$ (Å) | $\sigma^2$ (Å$^2$) | $\Delta E_0$ (eV) | Residual |
|---|---|---|---|---|---|---|
| Hematite (XRD) [56] | O | 6 | 1.95–2.12[b] | | | |
| | Fe | 1 | 2.90 | | | |
| | Fe | 3 | 2.97 | | | |
| | Fe | 3 | 3.36 | | | |
| | Fe | 6 | 3.71 | | | |
| Goethite (XRD) [57] | O | 6 | 1.93–2.10[c] | | | |
| | Fe | 6 | 3.01 | | | |
| | Fe | 6 | 3.29 | | | |
| | Fe | 12 | 3.43 | | | |
| Hematite | O | 6[a] | 2.03 ± 0.02 | 0.013 ± 0.001 | −0.99 ± 0.13 | 20.6 |
| | Fe | 4[a] | 2.95 ± 0.02 | 0.008 ± 0.001 | | |
| | Fe | 3[a] | 3.36 ± 0.02 | 0.002 ± 0.001 | | |
| Goethite | O | 6[a] | 1.97 ± 0.02 | 0.013 ± 0.001 | −4.53 ± 0.45 | 12.4 |
| | Fe | 6[a] | 3.04 ± 0.02 | 0.016 ± 0.002 | | |
| | Fe | 8.6 ± 3.4 | 3.35 ± 0.02 | 0.014 ± 0.001 | | |
| HFO | O | 6[a] | 2.03 ± 0.02 | 0.013 ± 0.002 | 3.39 ± 0.52 | 24.2 |
| | Fe | 3.6 ± 1.4 | 3.08 ± 0.02 | 0.013 ± 0.003 | | |
| Pb/HFO | O | 6[a] | 2.04 ± 0.02 | 0.013 ± 0.001 | 3.73 ± 0.96 | 25.0 |
| $10^{-3}$ mol/g, pH 6, IS $10^{-3}$ | Fe | 4.8 ± 1.9 | 3.06 ± 0.02 | 0.016 ± 0.001 | | |
| Pb/HFO, 21 months | O | 6[a] | 1.99 ± 0.02 | 0.013 ± 0.001 | −0.07 ± 0.37 | 24.2 |
| $10^{-3}$ mol/g, pH 5, IS $10^{-2}$ | Fe | 2.7 ± 1.1 | 3.06 ± 0.02 | 0.010 ± 0.001 | | |

*Note.* FT was performed over range: hematite 2.83–11.42 Å$^{-1}$, goethite 2.63–11.19 Å$^{-1}$, HFO and Pb/HFO sorption samples 2.86–11.77 Å$^{-1}$. Hematite was fitted over range 0.53–3.95 Å, goethite 0.63–3.76 Å, HFO and Pb/HFO samples 0.52–3.91 Å. $N$, coordination number; $R$, interatomic distance; $\sigma^2$, Debye–Waller factor; $\Delta E_0$, edge shift.

[a] Fixed $N$ numbers in fitting.
[b] 3 O at 1.95 Å; 3 O at 2.12 Å.
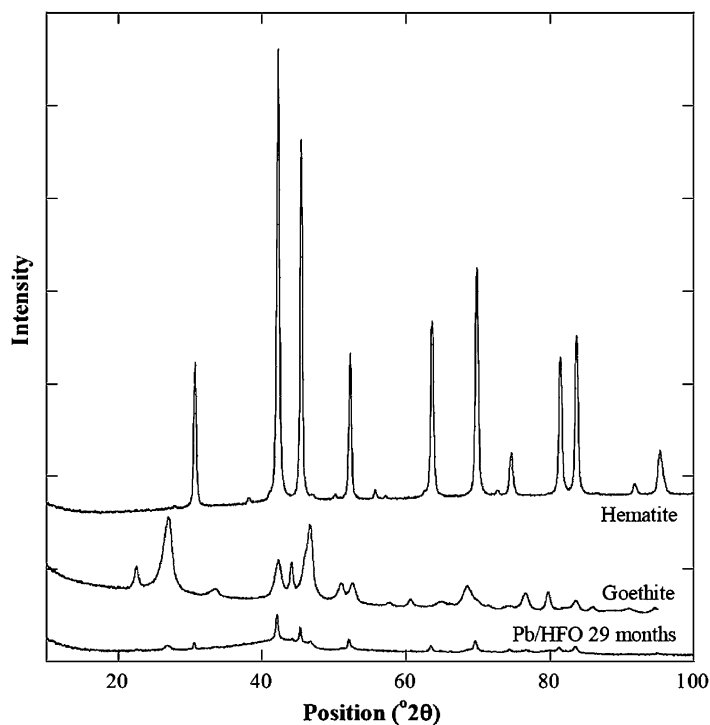[c] 2 O at 1.93 Å; 1 O at 1.95 Å; 1 O at 2.07 Å; 2 O at 2.10 Å.



Fig. 5. XRD analyses of long-term Pb/HFO sample (sample aged for 29 months) compared with those of hematite and goethite.

Fits were not obtained with Pb in the second shell, therefore Pb(II) ions do not appear to substitute into Fe positions in freshly prepared HFO even with a Pb/Fe molar ratio of 0.37

(corresponding to $3.41 \times 10^{-3}$ mol Pb/g HFO) or aged for 21 months. The similarity in EXAFS results of 4-h and 21-month Pb/HFO with pure HFO suggests that HFO does not transform

into a more crystalline form in the presence of Pb(II) during aging up to 21 months. The adsorbed Pb(II) ions binding to the edges of HFO polymers may block the edge and corner-sharing between HFO polymers thus inhibiting crystal growth. This observation is important for situations where adsorption occurs not long after ferric oxide precipitation (possibly in wastewater treatment), the large binding capacity of the amorphous oxide is maintained resulting in more effective removal of Pb(II).

### 3.3. Pb EXAFS of Pb/HMO samples

Similar to HFO, HMO also is an important surface in the environment. A large amount of internal adsorption sites exist on the micropore walls because of the large porosity of HMO [35]. EXAFS analysis was conducted on short-term and long-term Pb/HMO samples to investigate adsorption mechanisms.

The EXAFS spectra of all Pb/HMO samples (Fig. 6) show similar patterns suggesting one type of adsorption mechanism
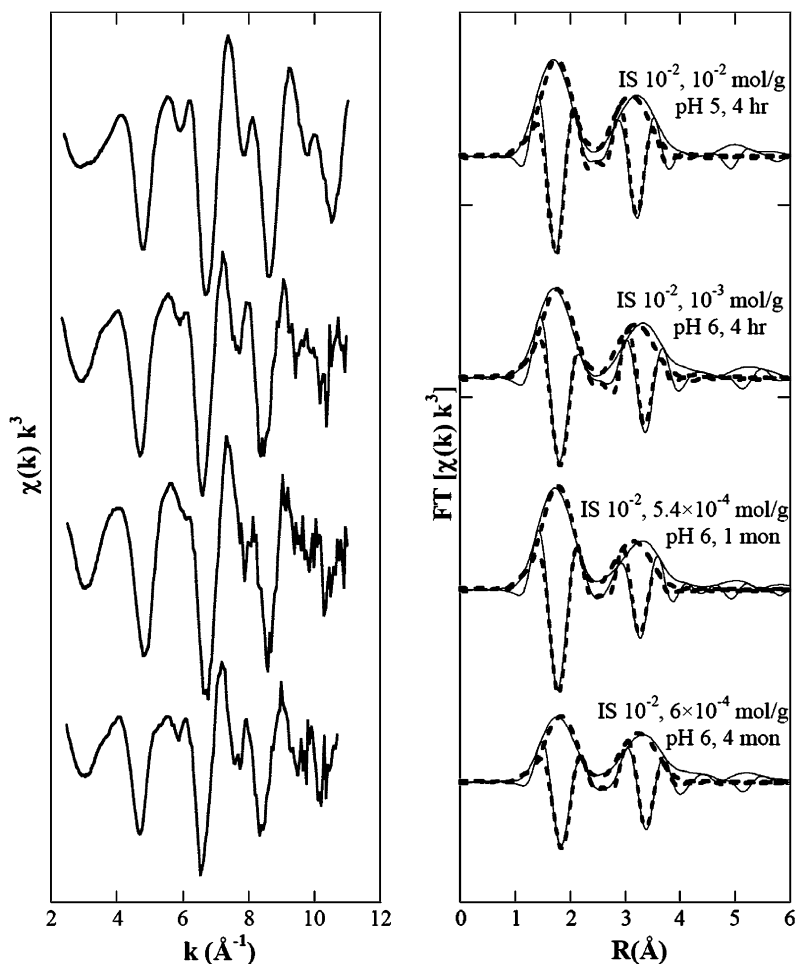


Fig. 6. EXAFS spectra and Fourier transform (magnitude and imaginary part) of Pb/HMO samples at Mn K-edge. FT was performed over range 2.66–10.56 Å$^{-1}$, fitted over range 0.58–4.8 Å. Dashed lines represent fits.

Table 5
EXAFS results of Pb/HMO samples at Pb L$_{III}$-edge: FT was performed over range 2.66–10.56 Å$^{-1}$, fitted over range 0.58–4.8 Å for all Pb/HMO samples

| Sample | Atom | $N$ | $R$ (Å) | $\sigma^2$ (Å$^2$) | $\Delta E_0$ (eV) | Residual |
|---|---|---|---|---|---|---|
| Pb/HMO | O | $2.0 \pm 0.4$ | $2.28 \pm 0.02$ | $0.004 \pm 0.001$ | $-11.0 \pm 0.2$ | 21.7 |
| $10^{-2}$ mol/g, pH 5, IS $10^{-2}$ | Mn | $1.4 \pm 0.6$ | $3.65 \pm 0.02$ | $0.005 \pm 0.001$ | | |
| Pb/HMO | O | $2.2 \pm 0.4$ | $2.32 \pm 0.02$ | $0.008 \pm 0.001$ | $-10.2 \pm 1.2$ | 24.6 |
| $10^{-3}$ mol/g, pH 6, IS $10^{-2}$ | Mn | $1.1 \pm 0.4$ | $3.72 \pm 0.02$ | $0.003 \pm 0.003$ | | |
| Pb/HMO, 1 month | O | $2.7 \pm 0.6$ | $2.30 \pm 0.02$ | $0.007 \pm 0.001$ | $-8.7 \pm 1.9$ | 20.6 |
| $5.4 \times 10^{-3}$ mol/g, pH 6, IS $10^{-2}$ | Mn | $1.2 \pm 0.5$ | $3.67 \pm 0.05$ | $0.005 \pm 0.002$ | | |
| Pb/HMO, 4 months | O | $1.8 \pm 0.4$ | $2.35 \pm 0.02$ | $0.007 \pm 0.001$ | $-5.8 \pm 0.8$ | 19.2 |
| $5.4 \times 10^{-3}$ mol/g, pH 6, IS $10^{-2}$ | Mn | $1.9 \pm 0.8$ | $3.76 \pm 0.02$ | $0.008 \pm 0.001$ | | |

*Note.* $N$, coordination number; $R$, interatomic distance; $\sigma^2$, Debye–Waller factor; $\Delta E_0$, edge shift. An $S_0^2$ of 0.91 was used to account for self-absorption based on the ratio of fluorescence to transmission data for aqueous Pb$^{2+}$.

as a function of pH, ionic strength, loading, and reaction time (from 4 h to 4 months). This observation is consistent with that for the Pb/HFO system. The beat features suggest the presence of a second shell consisting of heavier atoms and is clearly seen in the RSF (Fig. 6) as a well-defined peak beyond the first shell. The fitting results (Table 5) reveal 1.8–2.7 O atoms at 2.28–2.35 Å for the first shell and 1.1–1.9 Mn atoms at 3.65–3.76 Å for the second shell. The Pb–O distances on HMO are similar to those on HFO surface (2.25–2.30 Å). The second shell can be successfully fit only with Mn; trials with two Gaussian subshells of Mn related to single- and double-corner-sharing complexes did not result in a physically meaningful fit. Matocha et al. [26] assigned a Pb–Mn distance of 3.74 Å for Pb/birnessite to a corner-sharing Pb complex coordinated above and below the vacancy sites on birnessite. Using three subshells and fixing their coordination numbers for the second shell, Villalobos et al. [27] resolved Pb–Mn distances of ∼3.5, 3.7, and 5.5 Å for Pb sorbed to a layered biogenic manganese oxide; the authors attributed the results to double-corner- and triple-corner-sharing complexes at the external and interlayer sites respectively. In this study, all fitting parameters were floated (except $S_0^2$ was fixed at 0.91, Table 5) due to the highly disordered HMO structure [61]. The Pb–Mn distance of 3.65–3.76 Å suggests double-corner-sharing complexes.

Pb(II) sorbed on birnessite [23,25,26] shows Pb–O distance of 2.23–2.38 Å and Pb–Mn distances of 3.74–3.77 Å. Considering the error, the local structure of Pb(II) on HMO surface obtained in this study is similar to those on crystalline Mn oxides. In other words, Pb(II) ions form mononuclear corner-sharing surface complexes on both amorphous and crystalline Mn oxides. This observation is not surprising because, similar to iron oxides, amorphous HMO has been found to exhibit a short-range structure of edge- and corner-sharing $MnO_6$ octahedra with local structure resembling those of well-crystallized (oxyhydr)oxides [23,52,54,55,57].

The similarity in $\chi(k)k^3$ spectra and the fitting results of 4-h and 4-month samples indicate alike local structures. Therefore, consistent with the results for HFO, the internal and external Pb adsorption sites on HMO are approximately equivalent. The assumption used in earlier modeling efforts [32,33,36,38], which is that adsorption sites located along the micropore walls are no different from ones on the external surface, is also corroborated in this current Pb/HMO EXAFS study.

### 3.4. Intraparticle surface diffusion modeling

Results for Pb/HFO adsorption at pH 5 (Fig. 7) showed that approximately 77% sorbed within 4 h (Fig. 7, insert).
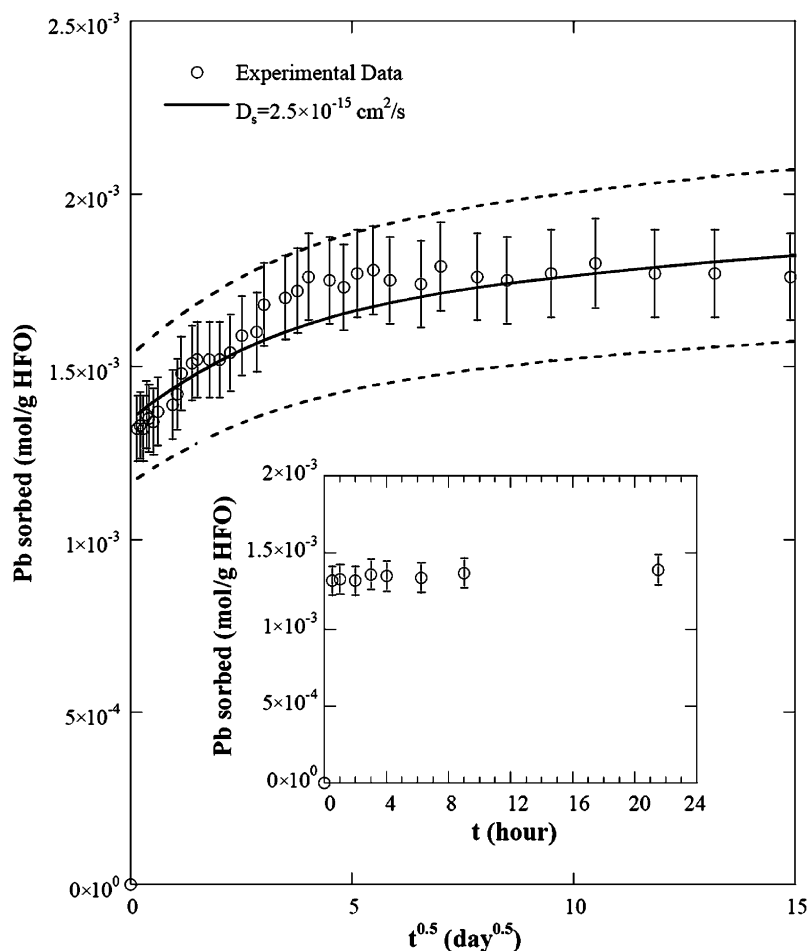


Fig. 7. Pb/HFO CBC study on 0.3 g L$^{-1}$ HFO at IS = $1.4 \times 10^{-2}$, pH 5, and [Pb]$_{eq}$ = $1 \times 10^{-4}$ M. Dashed lines represent the error (±two standard deviation) of the model.

This fraction represents that sorbed to the external surface of the freshly precipitated HFO. The remaining Pb was sorbed through a much slower process—intraparticle surface diffusion. As discussed earlier, this slow process was observed by maintaining a constant boundary condition of the Pb(II) in the bulk aqueous phase and therefore on the external surface. This slow adsorption process was observed for over 10 months.

The above XAS results suggest that, in the presence of Pb(II), HFO remains in amorphous form for up to 21 months; furthermore, Pb adsorption is invariant as a function of time, pH, and ionic strength. These findings support the assumption that sites located on the micropore walls may be characterized as equivalent to those on the external surface; this approach has been demonstrated in early studies as well [17,24,32,33,35,36, 38] in modeling intraparticle surface diffusion along micropore walls. Therefore, integrating the analytical solution over a spherical particle results in the amount of Pb sorbed to the internal surface of a single particle at a given time [32,33,36,38]. The moles ($M$) sorbed internally is expressed below:

$$M = 4\pi C_s \frac{R^3}{3} \left[ 1 - \frac{6}{\pi^2} \sum_{n=1}^{\infty} \frac{1}{n^2} \exp\left( -\frac{Dn^2\pi^2 t}{R^2} \right) \right], \quad (1)$$

$$D = \frac{D_s}{1 + (\varepsilon'/\rho K_i)}, \quad (2)$$

where $C_s$ is the metal concentration sorbed on the oxide external surface, $R$ is the radius of the particle, $\varepsilon$ is the oxide porosity, $\rho$ is the bulk density, $K_i$ is the distribution coefficient representing the equilibrium constant times the internal site density, and $D_s$ is the surface diffusivity.

The amount of Pb sorbed along the micropores times the number of particles with that radius was summed over the entire particle size distribution to obtain the total Pb concentration sorbed internally. The summation of Pb sorbed internally and externally provides the theoretical value of the total Pb sorbed. $D_s$ is the only fitting parameter in the modeling process. The best-fit $D_s$ is obtained by minimizing the variance between that theoretically sorbed and the experimental data. Modeling results for Pb/HFO CBC experiment are shown as an example (Fig. 7). The experimental data fall within two standard deviations of the model suggesting that the diffusion model fits data reasonably well. The best-fit $D_s$ was $2.5 \times 10^{-15}$ cm$^2$ s$^{-1}$ suggesting a slow and rate-limiting process for Pb sorption to HFO. Results from many studies support that intraparticle diffusion is the rate-limiting step in metal sorption to microporous oxides [17,24,31–34,36–38,58]. The $D_s$ of this study ($2.5 \times 10^{-15}$ cm$^2$ s$^{-1}$) is consistent with the range obtained by Fan et al. [38] for Pb sorption in HAO, HMO, and HFO ($10^{-16}$–$10^{-14}$ cm$^2$ s$^{-1}$).

Because HFO is metastable, the rate of its structural transformation requires further investigation. After 29 months of aging, XRD analysis (Fig. 5) suggests the dominance of ferrihydrite with trace hematite and goethite. As shown by Ainsworth et al. [62] and Ford et al. [63,64], Pb partitioning to HFO is dominated by adsorption irrespective of transformation to more stable iron oxides. However, desorption of Pb may occur if its loading exceeds the adsorption capacity of the crystalline oxide.

Similarly, the level-out of the experimental data (Fig. 7) may be explained with possible changes in HFO site density (both internal and external) caused by the structural rearrangement of HFO at micro- or nanometer level.

## 4. Summary

Pb(II) adsorption mechanisms on freshly precipitated HFO and HMO samples as a function of time have been studied. XAS results reveal that the freshly precipitated HFO exhibits short-range order possibly forming edge-sharing polymers. The sorbed Pb(II) ions do not substitute for Fe in the polymer structure. However, by binding to the edges of octahedra polymers, Pb(II) ions inhibit crystallization of HFO which is stable up to 21 months of aging, thus maintaining its large capacity for Pb(II). EXAFS analysis of both Pb(II)-sorbed amorphous HFO and HMO samples suggest that Pb(II) ions form mononuclear bidentate surface complexes on FeO$_6$ and MnO$_6$ octahedra. These similar adsorption mechanisms appear to be invariant of pH, ionic strength, Pb loading, and reaction time. Pb adsorption on HFO is a two-step process—a fast initial uptake followed by a slow surface diffusion step. The adsorption mechanism does not appear to change with reaction time (as long as 21 and 4 months for HFO and HMO, respectively) suggesting that internal sites on micropore walls are no different than the external surface ones. Intraparticle surface diffusion modeling based on this observation described the Pb/HFO long-term adsorption data reasonably well. The surface diffusivity obtained from the modeling verifies a slow and rate-limiting diffusion process. Results from this study help in eliciting adsorption mechanisms of heavy metals, e.g., Pb(II), to hydrous Fe and Mn oxides, and can be applied to surface complexation as well as intraparticle surface diffusion modeling, which can then be combined for improved geochemical transport depiction.

## References

[1] P.R. Anderson, T.H. Christensen, J. Soil Sci. 39 (1988) 15–22.
[2] R.E. Jackson, K.J. Inch, J. Contam. Hydrol. 4 (1989) 27–50.

[3] C.C. Fuller, J.A. Davis, J.A. Coston, E. Dixon, J. Contam. Hydrol. 22 (1996) 165–187.

[4] H. Green-Pedersen, B.T. Jensen, N. Pind, Environ. Technol. 18 (1997) 807–815.

[5] D. Dong, L.A. Derry, L.W. Lion, Water Res. 37 (2003) 1662–1666.

[6] A. Manceau, M.C. Boisset, G. Sarret, J.L. Hazemann, M. Mench, P. Cambier, R. Prost, Environ. Sci. Technol. 30 (1996) 1540–1552.

[7] P.A. O'Day, S.A. Carroll, G.A. Waychunas, Environ. Sci. Technol. 32 (1998) 943–955.

[8] J.D. Ostergren, T.P. Trainor, J.R. Bargar, G.E. Brown Jr., G.A. Parks, J. Colloid Interface Sci. 225 (2000) 466–482.

[9] J.D. Ostergren, G.E. Brown Jr., G.A. Parks, P. Persson, J. Colloid Interface Sci. 225 (2000) 483–493.

[10] J.R. Bargar, S.N. Towle, G.E. Brown Jr., G.A. Parks, Geochim. Cosmochim. Acta 60 (1996) 3541–3547.

[11] J.R. Bargar, G.E. Brown Jr., G.A. Parks, Geochim. Cosmochim. Acta 61 (1997) 2617–2638.

[12] J.R. Bargar, G.E. Brown Jr., G.A. Parks, Geochim. Cosmochim. Acta 61 (1997) 2639–2652.

[13] J.R. Bargar, G.E. Brown Jr., G.A. Parks, Geochim. Cosmochim. Acta 62 (1998) 193–207.

[14] C.J. Chisholm-Brause, A.L. Roe, K.F. Hayes, G.E. Brown Jr., G.A. Parks, J.O. Leckie, Physica B Condens. Matter 158 (1989) 674–675.

[15] C.J. Chisholm-Brause, K.F. Hayes, L.A. Roe, G.E. Brown Jr., G.A. Parks, J.O. Leckie, Geochim. Cosmochim. Acta 54 (1990) 1897–1909.

[16] A.L. Roe, K.F. Hayes, C. Chisholm-Brause, G.E. Brown Jr., G.A. Parks, K.O. Hodgson, J.O. Leckie, Langmuir 7 (1991) 367–373.

[17] D.G. Strawn, A.M. Scheidegger, D.L. Sparks, Environ. Sci. Technol. 32 (1998) 2596–2601.

[18] J.D. Ostergren, J.B. Bargar, G.E. Brown Jr., G.A. Parks, J. Synch. Rad. 6 (1999) 645–647.

[19] J.D. Ostergren, G.E. Brown Jr., G.A. Parks, T.N. Tingle, Environ. Sci. Technol. 33 (1999) 1627–1636.

[20] E.J. Elzinga, D. Peak, D.L. Sparks, Geochim. Cosmochim. Acta 65 (2001) 2219–2230.

[21] A.S. Templeton, A.M. Spormann, G.E. Brown Jr., Environ. Sci. Technol. 37 (2003) 2166–2172.

[22] P. Trivedi, J.A. Dyer, D.L. Sparks, Environ. Sci. Technol. 37 (2003) 908–914.

[23] A. Manceau, L. Charlet, M.C. Boisset, B. Didier, L. Spadini, Appl. Clay Sci. 7 (1992) 201–223.

[24] A.C. Scheinost, S. Abend, K.I. Pandya, D.L. Sparks, Environ. Sci. Technol. 35 (2001) 1090–1096.

[25] A. Manceau, B. Lanson, V.A. Drits, Geochim. Cosmochim. Acta 66 (2002) 2639–2663.

[26] C.J. Matocha, E.J. Elzinga, D.L. Sparks, Environ. Sci. Technol. 35 (2001) 2967–2972.

[27] M. Villalobos, J. Bargar, G. Sposito, Environ. Sci. Technol. 39 (2005) 569–576.

[28] S. Kuo, D.S. Mikkelsen, Soil Sci. 128 (1979) 274–277.

[29] R.G. Lehmann, R.D. Harter, Soil Sci. Soc. Am. J. 48 (1984) 769–772.

[30] N.J. Barrow, J. Soil Sci. 37 (1986) 277–286.

[31] T.L. Theis, R. Lyer, S.K. Ellis, Environ. Progress 13 (1994) 72–77.

[32] L. Axe, P.R. Anderson, J. Colloid Interface Sci. 175 (1995) 157–165.

[33] L. Axe, P.R. Anderson, J. Colloid Interface Sci. 185 (1997) 436–448.

[34] C. Papelis, P.V. Roberts, J.O. Leckie, Environ. Sci. Technol. 29 (1995) 1099–1108.

[35] P. Trivedi, L. Axe, J. Colloid Interface Sci. 218 (1999) 554–563.

[36] P. Trivedi, L. Axe, Environ. Sci. Technol. 35 (2001) 1779–1784.

[37] T.J. Strathmann, S.C.B. Myneni, Environ. Sci. Technol. 39 (2005) 4027–4034.

[38] M. Fan, T. Boonfueng, Y. Xu, L. Axe, T.A. Tyson, J. Colloid Interface Sci. 281 (2005) 39–48.

[39] P. Trivedi, L. Axe, J. Colloid Interface Sci. 244 (2001) 221–229.

[40] D.A. Dzombak, F.M.M. Morel, J. Colloid Interface Sci. 112 (1986) 588–598.

[41] R.R. Gadde, H.A. Laitinen, Anal. Chem. 46 (1974) 2022–2026.

[42] C.F. Baes Jr., R.E. Mesmer, The Hydrolysis of Cations, Wiley, New York, 1976.

[43] J.C. Westall, J.L. Zachary, F.M.M. Morel, MINEQL. A computer program for the calculation of the chemical equilibrium composition of aqueous systems, Report 86-01, Department of Chemistry, Oregon State University, Corvalis, OR, 1986.

[44] B. Bunker, D. Sayers, in: D.C. Koningsberger, R. Prins (Eds.), X-Ray Absorption: Principles, Applications, Techniques of EXAFS, SEXAFS, and XAFS, Wiley, New York, 1988.

[45] S.I. Zabinsky, J.J. Rehr, A. Ankudinov, R.C. Albers, M.J. Eller, J. Phys. Rev. B Condens. Matter 52 (1995) 2995–3009.

[46] JCPDS. Mineral Powder Diffraction File Databook, Sets 1–42, International Center for Diffraction Data: Swarthmore, PA, 1993.

[47] H. Stanjek, P.G. Weidler, Clay Miner. 27 (1992) 397–412.

[48] E.J. Elzinga, D.L. Sparks, Environ. Sci. Technol. 36 (2002) 4352–4357.

[49] U. Schwertmann, P. Cambier, E. Murad, Clays Clay Miner. 33 (1985) 369–378.

[50] R.M. Cornell, Z. Pflanzenernaehr. Bodenkd. 150 (1987) 304–307.

[51] R.M. Cornell, R. Giovanoli, P.W. Schindler, Clays Clay Miner. 35 (1987) 21–28.

[52] J.M. Combes, A. Manceau, G. Calas, J.Y. Bottero, Geochim. Cosmochim. Acta 53 (1989) 583–594.

[53] A. Szytula, A. Burewicz, Z. Dimitrijevic, S. Krasnicki, H. Rzany, J. Todorovic, A. Wanic, W. Wolski, Phys. Status Solidi 26 (1968) 429–434.

[54] A. Manceau, J.M. Combes, Phys. Chem. Miner. 15 (1988) 283–295.

[55] J.M. Combes, A. Manceau, G. Calas, Geochim. Cosmochim. Acta 54 (1990) 1083–1091.

[56] L. Charlet, A.A. Manceau, J. Colloid Interface Sci. 148 (1992) 443–458.

[57] A. Manceau, V. Drits, Clay Miner. 28 (1993) 165–184.

[58] G.A. Waychunas, B.A. Rea, C.C. Feller, J.A. Davis, Geochim. Cosmochim. Acta 57 (1993) 2251–2269.

[59] R.L. Blake, R.E. Hessevick, T. Zoltai, L.W. Finger, Am. Mineral. 51 (1966) 123–129.

[60] A. Gualtieri, P. Venturelli, Am. Mineral. 84 (1999) 895–904.

[61] T. Boonfueng, L. Axe, Y. Xu, J. Colloid Interface Sci. 281 (2005) 80–92.

[62] C.C. Ainsworth, J.L. Pilon, P.L. Gassman, W.G. Van Der Sluys, Soil Sci. Soc. Am. J. 58 (1994) 1615–1623.

[63] R.G. Ford, P.M. Bertsch, K.J. Farley, Environ. Sci. Technol. 31 (1997) 2028–2033.

[64] R. Ford, K.M. Kemner, P.M. Bertsch, Geochim. Cosmochim. Acta 63 (1999) 39–48.

[65] R.J. Hill, Acta Cryst. C 41 (1985) 1281–1284.

[66] K.Z. Sahl, Kristallographie 139 (1974) 215–222.